

Signatures of Galaxy-Cluster Interactions: Tully-Fisher Observations at $z \sim 0.1$

Daniel A. Dale

Department of Physics and Astronomy, University of Wyoming, Laramie, WY 82071

and

Juan M. Uson

*National Radio Astronomy Observatory, 520 Edgemont Road, Charlottesville, VA 22903***ABSTRACT**

We have obtained new optical imaging and spectroscopic observations of 78 galaxies in the fields of the rich clusters Abell 1413 ($z = 0.14$), Abell 2218 ($z = 0.18$) and Abell 2670 ($z = 0.08$). We have detected line emission from 25 cluster galaxies plus an additional six galaxies in the foreground and background, a much lower success rate than what was found (65%) for a sample of 52 lower-richness Abell clusters in the range $0.02 \lesssim z \lesssim 0.08$. We have combined these data with our previous observations of Abell 2029 and Abell 2295 (both at $z = 0.08$), which yields a sample of 156 galaxies. We evaluate several parameters as a function of cluster environment: Tully-Fisher residuals, $H\alpha$ equivalent width, and rotation curve asymmetry, shape and extent. Although $H\alpha$ is more easily detectable in galaxies that are located further from the cluster cores, we fail to detect a correlation between $H\alpha$ extent and galaxy location in those where it is detected, again in contrast with what is found in the clusters of lesser richness. We fail to detect any statistically significant trends for the other parameters in this study. The zero-point in the $z \sim 0.1$ Tully-Fisher relation is marginally fainter (by 1.5σ) than that found in nearby clusters, but the scatter is essentially unchanged.

Subject headings: galaxies: clusters: individual (Abell 1413, Abell 2218, Abell 2670) — galaxies: distances and redshifts — galaxies: evolution — cosmology: observations

1. Introduction

Galaxies in dense clusters evolve mainly due to tidal interactions, mergers and ram pressure stripping with accretion contributing to the buildup of the cD galaxies that often reside at the bottom of the cluster potential (Dressler 1984). These processes are expected to be most effective in the cluster cores where higher densities will lead to more efficient ram pressure stripping and

tidal effects should be stronger. Indeed, observations of $H\alpha$ in Abell 2029 failed to detect emission-line galaxies projected within $600 h_{70}^{-1}$ kpc of the center of the cluster, with the exception of a background galaxy, whereas two-thirds of the galaxies located outside this radius were detected (Dale & Uson 2000).

It is well established that galaxies in clusters tend to be deficient in their neutral Hydrogen (H I) emission (e.g. Haynes, Giovanelli & Chincarini 1984). More recently, Solanes et al. (2001) analyzed a sample of 1900 galaxies in the fields of eighteen nearby clusters ($z \lesssim 0.04$) and found that H I deficient galaxies are more likely located near the cluster cores. This trend holds true in Abell 2670, which is one of the most distant clusters to be imaged in neutral Hydrogen ($z \sim 0.08$, van Gorkom 1996). A truly extreme case is that of Abell 2029 which is at the same redshift as Abell 2670 but in which a deeper search for H I by one of us (JMU) resulted in an order of magnitude lower detection rate. H I deficiency in cluster galaxies is usually attributed to ram pressure stripping: as galaxies approach the central regions of clusters at a speed v , they experience a strong interstellar-gas–intracluster-gas interaction which is proportional to v^2 . This interaction is likely to induce a burst of star formation and subsequently strip away most of the the remaining galactic interstellar gas (Fujita 1998; Fujita & Nagashima 1999; Balogh et al. 1999; Quilis, Moore & Bower 2000).

New results from the Sloan Digital Sky Survey show cluster effects that cannot be reconciled by the morphology-density relation alone. Using a volume-limited sample of 8598 galaxies with $0.05 < z < 0.095$, Gomez et al. (2003) find that the galaxy star formation rate decreases with increasing galaxy density. In a study of the rotation curves of 510 galaxies in 53 clusters spread throughout $0.02 \lesssim z \lesssim 0.08$, Dale et al. (2001) found support for this galaxy-cluster interaction scenario in the normalized radial extent of $H\alpha$ emission in cluster spiral galaxies: it increases $4\pm 2\%$ per Mpc of (projected) separation of the galaxy from the cluster-core. Analysis of the kinematical asymmetries of the galaxies also shows a trend with cluster-centric distance—rotation curve asymmetry is greater by a factor of two for inner cluster early-type spiral galaxies. These two results lead these authors to claim that “*such trends are consistent with spiral disk perturbations or even the stripping of the diffuse, outermost gaseous regions within the disks as galaxies pass through the dense cluster cores*” (Dale et al. 2001).

Are such observables different in $z \sim 0.1$ clusters? Are they different for richer, more X-ray luminous clusters, thus solidifying the interpretation that the intracluster environment can significantly impact galaxy evolution in clusters? In an effort to explore the Tully-Fisher relation at $z \sim 0.1$, we have undertaken a new imaging and spectroscopic campaign of four rich Abell clusters: Abell 1413, Abell 2029, Abell 2218, and Abell 2670. Results from the first cluster surveyed, Abell 2029, were presented in Dale & Uson (2000). Here, we present a full analysis of the data for all four clusters. We also include results from Abell 2295, the only $z \sim 0.08$ cluster observed in the Dale et al. (1999) survey.

2. The Sample

Our sample consists of four Abell clusters that are among the densest and richest in the Abell catalog, thus providing good laboratories in which to study the effects of the intracluster medium and a fifth one (Abell 2295) of similar redshift but much lower richness (Table 1). We first discuss the three clusters for which new data have been obtained, and then the two clusters for which our data have already been published.

Abell 1413: Abell 1413 is a spiral rich cluster which harbors a dense core of galaxies and an extremely large cD galaxy at the bottom of the cluster potential well. Indeed, recent R band photometry shows that the cD halo extends over 1 Mpc from the cluster center (Uson and Boughn, in preparation). The average redshift is $cz_{\odot} = 42453 \pm 570 \text{ km s}^{-1}$ based on 9 measurements, and the velocity dispersion is $\sigma_{1d,rest} = 1490 \text{ km s}^{-1}$ (after correction for the cosmological broadening), which is highly uncertain given the small number of redshifts available for this cluster. Abell (1958) estimated its distance to be larger than it has turned out to be, because the stripping of the outer envelopes of its galaxies due to their presumed evolution in the dense environment of this cluster has resulted in a fainter magnitude for the tenth-ranked galaxy, used by Abell to assign distances and counting radii. Given its redshift, Dressler (1978) repeated the “Abell count” and upgraded its richness to 4.5 (Abell estimated $R = 3$). A similar increase in the richness of Abell 2029 and Abell 2218 is noted below, as is a decrease in the derived richness of Abell 2670. Bad weather severely limited our data collection on Abell 1413. Nevertheless, it seemed to lack galaxies with useful $H\alpha$ emission—observations of several galaxies in this cluster yielded only two weak emission line detections.

Abell 2218: The most distant cluster in the sample is Abell 2218 at $z \sim 0.18$, a dense cluster (Dressler’s $R = 4.3$ vs. Abell’s $R = 4$) also quite rich in spiral galaxy candidates. Extensive photometric and spectroscopic studies have been performed on the gravitational lensing arclets near the core of this cluster, contributing to excellent mass models of the region (Kneib et al. 1996). Deep VRI mosaic images of this cluster detect diffuse intracluster light at the $0.5 \times 10^9 M_{\odot} h_{70}^2 \text{ kpc}^{-2}$ level which traces the dark matter in the cluster (Boughn et al. 2000). We used the redshifts available in NED to compute a velocity dispersion $\sigma_{1d,rest} \sim 2200 \text{ km s}^{-1}$ which seemed too high. Indeed, we have found that a number of the redshifts that appear in NED are not the standard cz , but are instead the relative velocities that would result in the measured spectra in a laboratory experiment; i.e., deduced using the special-relativistic Doppler expression, although this was not stated in the original reference (Ziegler et al. 2001). The expression for the special-relativistic Doppler effect should not be used over cosmological distances, because even if the Universe was “flat” it would only be so in one (comoving) time slice. Space-time is curved and relative velocities are ill-defined over cosmological distances. Observed quantities should be reported, which in this case should be cz (preferably heliocentric). Thus, we have corrected the Ziegler et al. (2001) “velocities” to cz and, after removing some duplications, we have derived an average redshift of $cz_{\odot} = 52514 \pm 170 \text{ km s}^{-1}$ and a velocity dispersion of $\sigma_{1d,rest} = 1437 \pm 100 \text{ km s}^{-1}$ with 93 redshifts within one Abell radius. This dispersion is reasonably consistent with the value of 1202 km s^{-1} derived by Kneib et al. (1995)

for the central region from the lens model of the arcs in Abell 2218.

Abell 2670: Abell 2670 is dominated by one of the largest cD galaxies known. Its richness was lowered by Dressler (1978) from $R = 3$ (Abell 1958) to $R = 1.4$. A large number of redshifts have been measured for this cluster, providing an average of $cz_{\odot} = 22841 \pm 60$ and a velocity dispersion of $\sigma_{1d,rest} = 900 \pm 40 \text{ km s}^{-1}$ based on 235 galaxies located within a radius of $3.6 h_{70}^{-1}$ Mpc of the cluster center. It has been noted that the cluster shows significant substructure and might still be merging (Bird 1994). A deep VLA study of Abell 2670 detected ~ 30 H I sources, although none is located near the cluster core (van Gorkom 1996). Emission line spectroscopy in the relatively H I-rich Abell 2670 provides an important contrast to similar work in H I-poor Abell 2029.

Abell 2029: Abell 2029 is one of the densest and richest clusters in the Abell catalog. The cluster is a textbook example of a compact, relaxed, cD cluster with high intracluster X-ray luminosity. The cD galaxy is one of the largest galaxies known, with low surface brightness emission detected out to a radius of $0.9 h_{70}^{-1}$ Mpc (Uson, Boughn & Kuhn 1991). The average redshift is $cz_{\odot} = 23220 \pm 170 \text{ km s}^{-1}$ based on 92 measurements of galaxies within $2.1 h_{70}^{-1}$ Mpc and the velocity dispersion is $\sigma_{1d,rest} = 1471 \pm 100 \text{ km s}^{-1}$ (we have corrected the value reported in Dale & Uson 2000 which was inadvertently lowered by an extra factor of $1 + z$).

Abell 2295: This field is spiral rich, comprised of two superimposed clusters well separated in redshift. The farther cluster ($z \sim 0.08$) is dubbed “Abell 2295,” while the nearer cluster ($z \sim 0.06$) is referred to as “Abell 2295b” in Dale et al. (1998). Although of low richness (Abell’s $R = 0$) it is the only cluster at a similar redshift to those in our sample for which H α rotation curves are available and it is included in this study for comparison with our sample. The average redshift is $cz_{\odot} = 24623 \pm 200 \text{ km s}^{-1}$ based on 9 measurements of galaxies within $2.1 h_{70}^{-1}$ Mpc and the velocity dispersion is $\sigma_{1d,rest} = 560 \pm 160 \text{ km s}^{-1}$.

3. Observations and Data Reduction

The observing techniques and data reduction for Abell 2295 and Abell 2029 are described in Dale et al. (1998) and Dale & Uson (2000), respectively. The data for Abell 1413, Abell 2218 and Abell 2670 were obtained and processed using essentially the same approach. This section will present only new data—those for Abell 1413, Abell 2218 and Abell 2670—whereas the data from all five clusters will be included in the discussion.

3.1. Optical Spectroscopy

Long-slit spectroscopy was carried out at the Palomar Observatory 5 m telescope (Table 2). The red camera of the Double Spectrograph (Oke and Gunn 1982) was used to observe the H α (6563 Å), [N II] (6548, 6584 Å), and [S II] (6717, 6731 Å) emission lines. The spatial scale of

CCD21 (1024^2 pixels) was $0''.468 \text{ pixel}^{-1}$. The combination of the $1200 \text{ lines mm}^{-1}$ grating and a $2''$ wide slit yielded a dispersion of $0.65 \text{ \AA pixel}^{-1}$ and a spectral resolution of 1.7 \AA (equivalent to 75 km s^{-1} at 6800 \AA). Depending on which clusters were to be observed, the blaze and grating angle were selected according to the expected redshifted wavelength of $\text{H}\alpha$.

Deep I and/or R band images (§ 3.2) were used to select candidate galaxies as well as to estimate their position angles for follow-up long-slit spectroscopy. The spectroscopic observing strategy usually began with a 10 to 15 minute test exposure on each target. This allowed an estimate of the exposure time required in order to adequately sample the outer disk regions. Furthermore, the test exposure determined whether the galaxy was even useful for our purposes: a galaxy may lie in the foreground or background of the cluster or it may contain little or no $\text{H}\alpha$ emission. If the galaxy was deemed useful, a sequence of follow-up exposures were taken, with each integration typically 15 to 30 minutes in duration. Line emission was detected in 31 of the 78 galaxies observed in the fields of Abell 1413, Abell 2218 and Abell 2670 (the detection rate was 26/52 for Abell 2029 and 13/26 for Abell 2295). The galaxies observed are listed in Table 3.

Rotation curves have been extracted as discussed in Dale et al. (1997, 1998). The $\text{H}\alpha$ emission line was used to map the rotation curve except in the case of the galaxy AGC 630625 (in Abell 2670) where the emission of the $[\text{N II}]$ line (6584 \AA) extends to a larger distance than that of the $\text{H}\alpha$ emission (“AGC” refers to the Arecibo General Catalog maintained by M. P. Haynes and R. Giovanelli). Small portions of the $\text{H}\alpha$ rotation curve of one galaxy (AGC 630571, again in Abell 2670) have been determined using data from the $[\text{N II}]$ rotation curve in order to provide information on the shape of the inner parts and to ensure a consistent estimate of the velocity width.

The rotation curves vary in physical extent, and more importantly, they do not all reach the optical radius, R_{opt} , the distance along the major axis to the isophote containing 83% of the I band flux. Extrapolations to the rotation curves, and hence adjustments to the velocity width, are made when the $\text{H}\alpha$ emission does not extend to R_{opt} . The resulting correction depends on the shape of the rotation curve and exceeded 4% for five galaxies: AGC 261226 ($\approx 15\%$) in Abell 2218, and AGC 630588 ($\approx 22\%$); AGC 630593 ($\approx 19\%$); AGC 630615 ($\approx 10\%$) and AGC 630625 ($\approx 6\%$) in Abell 2670. To recover the actual rotational velocity widths, a few more corrections are necessary. The additional corrections account for disk inclination, cosmological broadening, and the smearing of the velocity profile in the $2''$ slit width (Dale 1998).

Figure 1 is a display of the rotation curves observed in the fields of Abell 2218 and Abell 2670. Notice that the data are highly correlated due to seeing and guiding jitter. This is properly taken into account by the fitting routines (see Dale et al. 1997 and references therein for details). Table 4 below contains the complete set of spectroscopic data for the galaxies for which useful rotation curves were obtained. Detailed comments for some galaxies follow:

A2218-261226: Large rotation curve extrapolation.

A2218-261244: Foreground galaxy.

A2218-261712: Foreground galaxy.

A2218-261715: Foreground galaxy.

A2670-630571: [N II] patch over inner 3''; weak line emission; uncertain disk ellipticity; unfit for Tully-Fisher use.

A2670-630588: Large rotation curve extrapolation.

A2670-630593: Large rotation curve extrapolation; possible flux contamination from galaxy 42'' to the NNW; merger?

A2670-630607: Background galaxy.

A2670-630624: Foreground galaxy; note low i .

A2670-630625: Large rotation curve extrapolation.

A2670-630627: Foreground galaxy; center of light used for rotation curve spatial and kinematic center.

3.2. Optical Imaging

I band photometry of Abell 2218 was obtained for a different project by one of us (JMU) in collaboration with S. P. Boughn (Haverford) with the 0.9 m telescope on Kitt Peak National Observatory on 1998 April 20. They used the T2KA camera mounted at the f:7.5 Cassegrain focus which resulted in square pixels, 0''.68 on a side. The seeing was good, between 1''.1 and 1''.4, which resulted in an effective seeing of $\sim 1''.5$ due to the available pixel size. Two sets of nine partially overlapping frames plus an extra frame at the center were used to form a mosaic of about 35' (RA) by 36' (Dec). The mosaic has overlaps of about 3/4 of a frame between immediately adjacent frames. All frames were obtained with air masses between 1.21 and 1.25. The exposures lasted five minutes. The data were processed as discussed in Uson, Boughn and Kuhn (1991, hereafter UBK91). All frames were used to generate a “sky-flat” gain calibration frame. Since the cluster contains a diffuse halo that surrounds the central galaxy, an 8' by 8' area centered on the cluster was blanked on all the frames before using them to generate the sky flat as discussed in UBK91. Because the atmospheric extinction was low (the secant-law extinction had a slope of 0.06 mag/airmass) and the frames were obtained at an approximately constant airmass, no differential atmospheric correction was applied to the frames. Absolute calibration was done using stars from Landolt’s *UBVRI* secondary calibration list (Landolt 1983).

We observed Abell 2670 in the I band using the Palomar 1.5 m telescope on the night of September 19, 2001. We used the 2048² CCD13 camera mounted at the f:7.5 Cassegrain focus which resulted in square pixels, 0''.378 on a side. The seeing was good, about 1''.1, which resulted in an effective seeing of $\sim 1''.2$. We obtained two sets of nine partially-overlapping frames in a 3×3 square pattern plus two sets of five frames in a “plus sign” pattern (with half of the spatial offsets used in the previous arrangement), all of them centered on the cD galaxy. Secant law calibration was deduced from stars located on the cluster frames (0.055 ± 0.008 mag/airmass) and agreed with that determined from secondary Landolt standards. The observations were made at

airmasses between 1.4 and 2.5. The data were processed as described above, again cutting from each frame an $8'$ by $8'$ area centered on the cluster in order to obtain a “sky-flat” gain calibration frame. Details will be given elsewhere.

R band photometry of Abell 1413 was obtained for a different project by one of us (JMU) in collaboration with S. P. Boughn with the 0.9 m telescope on Kitt Peak National Observatory on 1998 April 17. They used the same setup as for the I band observations of Abell 2218 discussed above. The seeing was good, between $0''.9$ and $1''.3$, which resulted in an effective seeing of $\sim 1''.4$. Three sets of nine partially overlapping frames were used to form a mosaic of about $35'$ by $35'$. The mosaic has overlaps of about $3/4$ of a frame between immediately adjacent frames. All frames were obtained with air masses between 1.01 and 1.10 with exposures of 2.5 minutes. The data were processed in the same way as the data for Abell 2029, discussed in UBK91. Because the atmospheric extinction was reasonably low (the secant-law extinction had a slope of 0.16 mag/airmass) and the frames were obtained at an approximately constant airmass, no differential atmospheric correction was applied to the frames. Absolute calibration was done using five stars from Landolt’s $UBVRI$ secondary calibration list (Landolt 1983) which were observed four times each at airmasses between 1.12 and 1.16. The mosaic was used to select candidate galaxies for the spectroscopic observations. Because the weather prevented us from obtaining any adequate rotation curves for this cluster, the absence of I band photometry for this cluster is, sadly, not a problem at this time.

Flux estimation follows from the data reduction methods discussed in Dale et al. (1997, 1998) using both standard and customized IRAF packages. Cosmological k -corrections are applied according to Poggianti (1997). The relevant photometric data are listed in Table 5 with the first column matching that of Table 4.

4. Results

Plots of the sky distribution of the galaxies observed in Abell 2218 and Abell 2670 are displayed in the upper panels of Figure 2. The lower panels present galaxy redshifts versus their projected distances from the cluster centers. Combining our observations with those reported in the literature yields large redshift samples: $N_z = 93$ and $N_z = 235$ for Abell 2218 and Abell 2670, respectively. For Abell 2218 the mean CMB cluster redshift is $cz_{\text{cmb}} = 52,497_{-170}^{+128}$ km s $^{-1}$ and the (rest frame) velocity dispersion 1437 ± 100 km s $^{-1}$; for Abell 2670 the numbers are $cz_{\text{cmb}} = 22,494_{-29}^{+87}$ km s $^{-1}$ and $\sigma_{\text{rest}} = 895 \pm 40$ km s $^{-1}$. Projected cluster membership contours are derived using the results from the CNOC survey of galaxy clusters (Carlberg et al. 1997), scaled by the cluster velocity dispersions. The 3σ contour is indicated by the two solid curves in each lower panel; the dotted curves show the 2σ contours (see, for example, Balogh et al. 1999).

4.1. The Distribution of Emission-Line Galaxies

Only 45% (70 of 156) of the targeted galaxies were detected in $H\alpha$. A small subset of the non-detected galaxies might lie outside the $30,000 \text{ km s}^{-1} cz$ ranges probed (Table 1). In contrast, Dale et al. (1999) detected line emission in 65% (582 of 897) of their $0.02 \lesssim z \lesssim 0.06$ targets, using a nearly identical observational approach. This relatively low success rate is likely due to the higher density of the clusters discussed in this paper, although it might be due in part to target selection effects. Whereas Dale et al. (1999) almost exclusively targeted late-type cluster galaxies, it is more difficult to avoid targeting early-type galaxies in more distant clusters. Balogh et al. (2002), for example, profited from *Hubble Space Telescope* imaging to differentiate between early-types and late-type galaxies in Abell 1689 at $z = 0.18$: they find that more than 90% of the cluster spirals show $H\alpha$ emission, whereas less than 10% of the early-type galaxies are “securely detected” in $H\alpha$.

Figure 3 shows the distribution of the observed galaxies as a function of projected distance to their respective cluster centers. Because the clusters are of different richness, we have scaled the distances using R_{200} , the cluster radius where the mean interior density is 200 times the critical density, since that radius generally contains the virialized mass (e.g. Equation 8 in Carlberg et al. 1997). As pictured in Figure 3, there is a difference in the spatial distribution of galaxies with and without optical emission lines (the search was limited to $H\alpha$, [N II], and [S II]; see Table 3). The galaxies with no line emission are more concentrated towards the cluster centers, at a median projected distance of $0.36 R_{200}$, whereas the galaxies with line emission are found to lie further out, at a median projected distance at $0.47 R_{200}$. This result is similar to findings that the star formation rate in cluster galaxies increases for larger cluster-centric distances (Balogh et al. 1998; Lewis et al. 2002). Inspection of Figure 4 shows that our sample selection is skewed towards late-type spirals near the cluster cores, suggesting that the observed distribution of emission-line galaxies is not entirely due to cluster morphological segregation (e.g. Dressler et al. 1997), consistent with the findings of Balogh et al. (1998) and Lewis et al. (2002). Furthermore, the panels for the individual clusters show significant segregation in A2029, A2218 and especially in A1413 where no galaxies showed strong $H\alpha$ emission. Conversely, no segregation is apparent in the poorer clusters A2295 and A2670 (which although it contains a cD galaxy seems far from dynamical relaxation as discussed above).

4.2. Rotation Curve Asymmetry, Shape, and Extent

4.2.1. Rotation Curve Asymmetry

Galaxy-galaxy or galaxy-cluster interactions can disturb disk velocity fields (e.g. Conselice & Gallagher 1999), but since they are expected to regularize within a few rotation cycles, it is likely that rotation curve asymmetries reflect only the most recent interaction history (see Dale et al. 2001 and references therein). As much as half of all galaxies, in clusters and in the field, show

significant rotation curve asymmetries or lopsided H I profiles (e.g. Richter & Sancisi 1994; Haynes et al. 1998; Swaters et al. 1999).

To measure the global rotation curve asymmetry the total area between the kinematically-folded approaching and receding halves is normalized by the average area under the rotation curve:

$$\text{Asymmetry} = \frac{\sum \frac{||V(R)|-|V(-R)||}{\sqrt{\sigma^2(R)+\sigma^2(-R)}}}{\frac{1}{2} \sum \frac{|V(R)|+|V(-R)|}{\sqrt{\sigma^2(R)+\sigma^2(-R)}}} \quad (1)$$

where $\sigma(R)$ is the uncertainty in the data at radial position R . The sample preferentially includes inclined disk systems ($i \gtrsim 45^\circ$), implying that the asymmetry parameter is more sensitive to noncircular than nonplanar motions (Kornreich et al. 2000). The average asymmetry for $z \sim 0.1$ cluster galaxies, $12.6 \pm 1.2\%$, is similar to that for the sample of more than 400 cluster galaxies and more than 70 field galaxies at lower redshift ($14.0 \pm 0.4\%$ and $12.5 \pm 1.0\%$, respectively) studied by Dale et al. (1997). There are no statistically significant differences with (spiral) galaxy morphological type or cluster-centric distance (see Figure 4 and Table 6).

4.2.2. Rotation Curve Shape

The shape of galaxy rotation curves has been suggested to be a probe of environmental influences (e.g. Whitmore, Forbes & Rubin 1988) as the cluster environment may inhibit dark matter halo formation and galaxy-galaxy/galaxy-cluster interactions should lead to stripping of part of the halo mass. Rotation curve shape is well-studied for galaxies in nearby clusters (see Dale et al. 2001 and references therein).

An indication of the rotation curve shape in the outer disk region is the “outer gradient” parameter (OG) defined in Dale et al. (2001) as

$$OG(\%) = 100 \times \frac{V(R_{\text{opt}}) - V(0.5R_{\text{opt}})}{V(R_{\text{opt}})} \quad (2)$$

where $V = V_{\text{rot}} \sin i$ is the projected rotational velocity of the disk at inclination i . Figure 4 displays this parameter as a function of projected cluster-centric distance. The average outer gradient for all $z \sim 0.1$ cluster galaxies is $\langle OG \rangle = 11.1 \pm 1.2\%$; a similar value is found for the low redshift cluster and field galaxies ($10.1 \pm 0.4\%$ and $10.6 \pm 1.1\%$). There are no statistically significant differences with spiral galaxy morphological type or cluster-centric distance.

4.2.3. Rotation Curve Extent

Another possible indicator of prior environmental influences is the radial extent of the line emission in spiral disks. In contrast to the inner-galaxy matter, the more diffuse and peripheral

mass is less gravitationally bound and is more easily stripped. For example, H I-deficiency is common for inner-cluster galaxies (e.g. Solanes et al. 2001), and the outer disk star formation rate is clearly truncated in Virgo cluster galaxies (Koopmann & Kenney 2002).

To extract rotational velocities reliably, good spectroscopic data are needed in the outermost portions of the galaxy disks. Therefore, care was taken to obtain sufficiently deep integrations to ensure high signal-to-noise data for the outer portions of the rotation curves. For the lower redshift cluster sample of Dale et al. (2001), the average radial extent of the rotation curves, R_{cut} , for all cluster galaxies is $\langle R_{\text{cut}}/R_{\text{opt}} \rangle = 1.11 \pm 0.02$; similar values are found for early-type spirals, late-type spirals, and foreground and background spirals. For the $z \sim 0.1$ cluster sample, the mean ratio is $\langle R_{\text{cut}}/R_{\text{opt}} \rangle = 1.18 \pm 0.07$. Does the extent of measured emission depend on environment? Rubin, Waterman & Kenney (1999) found that to be the case for Virgo cluster spirals, though no quantitative result was given. Dale et al. (2001) find a mild trend, a $4.1 \pm 2.3\%$ increase per h_{100}^{-1} Mpc ($2.9 \pm 1.6\%$ increase per h_{70}^{-1} Mpc) of projected galaxy-cluster core separation. We have recomputed this trend using R_{200} for the clusters in their sample and find a more significant increase in the H α extent of $3.5 \pm 0.5\%$ per R_{200} . The third panel of Figure 4 shows the radial extent of the rotation curves versus cluster-centric distance. We find no clear trend, an increase of $5 \pm 14\%$ per R_{200} ($\sim 13 \pm 7\%$ per h_{70}^{-1} Mpc). However, as discussed in Section 4.1 above, it seems that a large fraction of the galaxies located near the centers of these clusters shows no emission lines, suggesting that passage through the cores might have stripped the galaxies of most of their gas rather than just trimming its spatial extent.

4.2.4. H α Equivalent Width

The 2dF cluster data confirmed that H α equivalent width (a proxy for the star formation rate) decreases with decreasing projected cluster-centric distance, and is not entirely due to morphological segregation in clusters (Lewis et al. 2002). Gavazzi et al. (2002) focused on late-types in an H α study of 369 Virgo and Coma/A1367 galaxies, and found this trend only occurred for the brighter subset in Virgo. No firm trend is seen in our data (fourth panel in Figure 4).

4.3. The Tully-Fisher Relation at $z \sim 0.1$

Dale & Uson (2000) made an initial study of the Tully-Fisher relation at $z \sim 0.1$ via deep optical imaging and spectroscopy of Abell 2029. Based on a sample of 14 cluster galaxies, the study hinted at a larger intrinsic Tully-Fisher scatter and a zero point equivalent to that found in nearby clusters. The current sample more comprehensively probes the $z \sim 0.1$ epoch—43 galaxies spread throughout four different cluster environments.

The Tully-Fisher data for all members of the $z \sim 0.1$ clusters are presented in Figure 5 (residuals as a function of cluster environment are portrayed in the bottom panel of Figure 4). The

morphological type offsets for early-type disk galaxies advocated by Giovanelli et al. (1997) and Dale et al. (1999) are applied: $\Delta m_T = -0.1$ mag for Sb types and $\Delta m_T = -0.32$ mag for types earlier than Sb. Included in the plot is the template relation obtained from the Dale et al. (1999) all-sky of sample 52 galaxy clusters at $0.02 \lesssim z \lesssim 0.06$:

$$y = -7.68[\pm 0.10]x - 20.905[\pm 0.020] \text{ mag} \quad (3)$$

where y is $M_I - 5 \log h_{100}$ and x is $\log W_{\text{cor}} - 2.5$. The uncertainty in the zero point is a combination of the standard statistical uncertainty (0.018 mag) and the “kinematical uncertainty” (0.009 mag) due to the typical peculiar motions of clusters (see § 3.1 of Dale et al. 1999). As explained below, the slope and its uncertainty were adopted from Giovanelli et al. (1997).

The data in the righthand panel of Figure 5 are additionally corrected for cluster population incompleteness bias. In short, because magnitude-limited imaging preferentially samples the brighter end of the cluster luminosity function, the observed Tully-Fisher slope is artificially too shallow and the zero point overluminous. To remove this effect on the zero point, Monte Carlo simulations have been performed to recover an effective true “parent population,” given the observed sample and the scatter in the Tully-Fisher relation (Dale et al. (1999). In addition, samples of nearby clusters can better probe the Tully-Fisher slope: a wide dynamic range (of rotational velocity widths) is more easily observed in a nearby sample; owing to the relative propinquity of the Giovanelli et al. (1997) sample ($z \lesssim 0.02$), and because the Giovanelli et al. (1997) prescriptions for extracting Tully-Fisher data are consistent with their approach, Dale et al. (1999) adopted the (bias corrected) Giovanelli et al. (1997) slope. If this I band slope from nearby clusters is incorporated into this study, the fully-corrected $z \sim 0.1$ Tully-Fisher relation is

$$y(z \sim 0.1) = -7.68[\pm 0.10]x - 20.800[\pm 0.065] \text{ mag.} \quad (4)$$

The zero point is based on data from Abell 2029, Abell 2295, and Abell 2670, and assumes that these three clusters are on average at rest in rest frame of the cosmic microwave background. The scatter in the (bias corrected) Tully-Fisher data for each cluster is listed in Table 7. Calculated with respect to the $z \sim 0.1$ Tully-Fisher zero point, the inferred peculiar motion for Abell 2218 is large. Alternatively, assuming that Abell 2218 is at rest with respect to the cosmic background radiation leads to a slightly fainter zero point in the Tully-Fisher relation at $z \sim 0.18$, about -20.55 mag. However, this is only a 2σ effect, and is thus not significant at this point.

5. Discussion and Summary

The goal of this survey is to investigate the impact that the intracluster medium has on galaxies residing in a range of cluster environments at $z \sim 0.1$. A total of 156 galaxies were

observed spectroscopically in five clusters ranging from rich, X-ray luminous systems to richness class 0 clusters undetected in X-rays. About half of the sample (45%) was detected in H α .

We observe no significant trend in the extent of H α emission as a function of cluster-centric distance. This is in sharp contrast to what is observed in the nearby cluster sample, particularly when the projected cluster-centric distance is expressed in units of R_{200} . We also fail to detect significant trends in rotation curve asymmetry, I band Tully-Fisher residuals, rotation curve shape, and H α equivalent width. The relatively small number of rotation curves obtained for the dense clusters might be the main reason for our inability to detect statistically significant trends with cluster richness or location within the clusters. However, it is also possible that the low H α detection rate is a consequence of ram pressure stripping of the galaxies as they traverse the cores of the clusters, so that the galaxies that we do detect in H α would have avoided the cluster cores irrespective of their projected cluster-centric separation. Indeed, a VLA study of Abell 2670 found ~ 30 H I sources, but *none* within $0.5 h_{70}^{-1}$ Mpc of the cluster center (van Gorkom 1996). But a deep VLA survey of Abell 2029, sensitive to a 5σ H I mass of $5 \times 10^8 M_{\odot}$ within $1.5 h_{70}^{-1}$ Mpc of the cluster center, has detected only three sources (Uson, in preparation).

There is a clear difference in the cluster-centric distribution of actively star-forming and quiescent galaxies, with the star-forming galaxies preferentially found more in the cluster peripheries. This result is perhaps not surprising, given that the well-known cluster morphology-density relation likely contributes to this effect. Although ground-based imaging precluded perfect sample selection, we strived to only observe spiral galaxies. Moreover, as can be seen in Figure 4, our sample selection appears to have been skewed towards late-type spirals near the cluster cores. Thus, if the morphology-density relation has contributed to our observed distribution of strong and weak H α emitters, our sample selection seems to have minimized its impact.

The zero-point in the $z \sim 0.1$ I band Tully-Fisher relation (Equation 4) is a bit fainter (by 1.5σ) than that observed for nearby clusters (Equation 3). The data for Abell 2218, even more distant at $z \sim 0.18$, are an additional 1.8σ fainter than the $z \sim 0.1$ template. Are these discrepancies related to the comparatively high redshift of the clusters? Is this discrepancy evidence of evolution or observational biases? It is unclear whether or not the difference is due to systematic effects in the observational program: though seeing effects push deprojected rotational velocity widths to artificially high values, “slit smearing” of the disk rotation profile conversely biases the widths low. In case the correction recipes applied are unfit at this relatively high redshift, the simulations and empirical prescriptions used to generate the correction recipes have been revisited. For example, Dale et al. (1997) have calibrated the effects of seeing on the inferred inclinations. They found a linear relation between the circularization of isophotes and the ratio of the seeing full-width half-maximum to face-on disk scale length η :

$$\epsilon_{\text{true}}/\epsilon_{\text{obs}} = 1 + 0.118 \eta, \tag{5}$$

where ϵ_{true} and ϵ_{obs} are the “intrinsic” and “observed” disk ellipticities. However, they only tested this relation for galaxies observed out to $z \sim 0.06$. Using a separate technique from that explored in

Dale et al. (1997), we are able to both reproduce the seeing correction of Dale et al. (1997) over their sample’s $z \lesssim 0.06$ redshift range, and find that it is applicable even for galaxies as distant as those in Abell 2218. In the simulations artificial, inclined disk galaxies (created using MKOBJECTS in the ARTDATA package of IRAF) are progressively smoothed such that they exhibit increasingly circular isophotes. Isophotal ellipses are fit to the simulated galaxies using the same techniques used for the observed galaxies. The relation first quantified by Dale et al. (1997) tends to non-linearity only when η exceeds 2.0, and all of the galaxies observed in Abell 2218 have this ratio less than 1.8.

Both the total and intrinsic scatter of the I band Tully-Fisher relation at $z \sim 0.1$ are similar to that in nearby clusters. The total scatter is comparable to that found in Giovanelli et al. (1997) and Dale et al. (1999): 0.35 and 0.38 mag, respectively. The intrinsic scatter in the Tully-Fisher relation is the portion that cannot be reconciled by measurement uncertainties. This parameter presumably reflects the various feedback mechanisms and range of parameter space involved in galaxy formation. Andersen et al. (2001) suggest that perhaps up to half of the intrinsic scatter can be accounted for if disk galaxies simply have an average inherent ellipticity of 0.05, a value they find for their sample of seven nearly face-on spiral galaxies. Compared to the ~ 0.25 mag intrinsic scatter found by Dale et al. (1999) in clusters at lower redshifts, there is no significant difference in the intrinsic I band Tully-Fisher scatter in these four clusters at $z \sim 0.1$. In short, no significant evolution in the I band Tully-Fisher properties of cluster galaxies appears to have occurred since $z \sim 0.1$.

We are grateful for the assistance Richard Cool provided in preliminary explorations for correlations with cluster X-ray data. We thank Steve Boughn for his permission to use the unpublished I -band observations of Abell 2029 and Abell 2218 and Heinz Andernach for his insight on the redshifts of Abell 2218. The comments of the referee helped to improve the presentation of this work. The results presented in this paper are based on observations carried out at the Palomar Observatory (PO) and at the Kitt Peak national Observatory (KPNO). The Hale Telescope at the PO is operated by the California Institute of Technology under a cooperative agreement with Cornell University and the Jet Propulsion Laboratory. KPNO is operated by the Association of Universities for Research in Astronomy, Inc., under a cooperative agreement with the National Science Foundation. This research has made use of the NASA/IPAC Extragalactic Database (NED) which is operated by the Jet Propulsion Laboratory, California Institute of Technology, under contract with NASA, and the Image Reduction and Analysis Facility (IRAF) which is distributed by the National Optical Astronomy Observatories, which are operated by the Association of Universities for Research in Astronomy, Inc., under a cooperative agreement with the National Science Foundation. The NRAO is a facility of the National Science Foundation which is operated under cooperative agreement by Associated Universities, Inc. The Digitized Sky Surveys were produced at the Space Telescope Institute under U.S. Government grant NAG W-2166. The images of these surveys are based on photographic data obtained using the Oschin Schmidt Telescope on Palomar Mountain and the UK Schmidt Telescope.

REFERENCES

- Abell, G. O. 1958, *ApJS*, 3, 211
- Andersen, D. R., Bershad, M. A., Sparke, L. S., Gallagher III, J. S. & Wilcots, E.M. 2001, *ApJ*, 551, L131
- Balogh, M. L., Schade, D., Morris, S. L., Yee, H. K. C., Carlberg, R. G., & Ellingson, E. 1998, *ApJ*, 504, L75
- Balogh, M. L., Morris, S. L., Yee, H. K. C., Carlberg, R. G. & Ellingson, E. 1999, *ApJ*, 527, 54
- Balogh M. L., Couch, W. J., Smail, I., Bower, R. G. & Glazebrook, K. 2002, *MNRAS*, 335, 10
- Bird, C. 1994, *ApJ*, 422, 480
- Boughn, S. P., Uson, J. M., Blount, C. D. & Gupta, G. 2000, *BAAS*, 32, 1499
- Carlberg, R. G., Yee, H. K. C. & Ellingson, E. 1997, *ApJ*, 478, 462
- Conselice, C. J. & Gallagher III, J. S. 1999, *AJ*, 117, 75
- Dale, D. A., Giovanelli, R., Haynes, M. P., Scodreggio, M., Hardy, E. & Campusano, L. 1997, *AJ*, 114, 455
- Dale, D. A., Giovanelli, R., Haynes, M. P., Scodreggio, M., Hardy, E. & Campusano, L. 1998, *AJ*, 115, 418
- Dale, D. A. 1998, Ph.D. thesis, Cornell University
- Dale, D. A., Giovanelli, R., Haynes, M. P., Hardy, E. & Campusano, L. 1999, *AJ*, 118, 1489
- Dale, D. A. & Uson, J. M. 2000, *AJ*, 120, 552
- Dale, D. A., Giovanelli, R., Haynes, M. P., Hardy, E. & Campusano, L. 2001, *AJ*, 121, 1886
- Dressler, A. 1978, *ApJ*, 226, 55
- Dressler, A. 1984, *ARA&A*, 22, 185
- Dressler, A., Oemler Jr., A., Couch, W. J., Smail, I., Ellis, R. S., Barger, A. J., Butcher, H., Poggianti, B. M. & Sharples, R. M. 1997, *ApJ*, 490, 577
- Ebeling, H., Edge, A. C., Fabian, A. C., Allen, S. W., Crawford, C. S. & Böhringer H. 1997, *ApJ*, 479, L101
- Fujita, Y. 1998, *ApJ*, 509, 587
- Fujita, Y. & Nagashima, M. 1999, *ApJ*, 516, 619

- Gavazzi, G., Boselli, A., Pedotti, P., Gallazzi, A. & Carrasco, L. 2002, *A&A*, 396, 449
- Giovanelli, R., Haynes, M. P., Herter, T., Vogt, N. P., da Costa, L. N., Freudling, W., Salzer, J. J. & Wegner, G. 1997, *AJ*, 113, 53
- Gomez, P.L., Nichol, R.C., Miller, C.J. et al. (2003) *ApJ*, 584, 210
- Haynes, M. P., Giovanelli, R. & Chincarini, G. L. 1984, *ARA&A*, 22, 445
- Haynes, M. P., Hogg, D. E., Maddalena, R. J., Roberts, M. S. & van Zee, L. 1998, *AJ*, 115, 62
- Jones, C. & Forman, W. 1999, *ApJ*, 511, 65
- Kennicutt, R.C. 1998, *ARA&A*, 36, 189
- Kneib, J.-P., Mellier, Y., Pelló, R. Miralda-Escudé, J., Le Borgne, J.-F., Böhringer, H. & Picat, J.-P. 1995, *ã*, 303, 27
- Kneib, J.-P., Ellis, R. S., Smail, I., Couch, W. J. & Sharples, R. M. 1996, *ApJ*, 471, 643
- Kogut, A. et al. 1993, *ApJ*, 419, 1
- Koopmann, R.A. & Kenney, J.D.P. 2002, *ApJ*, submitted, astro-ph/0209547
- Kornreich, D. A., Haynes, M. P., Lovelace, R. V. E. & van Zee, L. 2000, *AJ*, 120, 139
- Landolt, A. U. 1983, *AJ*, 88, 439
- Lewis, I., et al. 2002, *MNRAS*, 334, 673
- Magri, C., Haynes, M. P., Forman, W., Jones, C. & Giovanelli, R. 1988, *ApJ*, 333, 136
- Oke, J. B. & Gunn, J. E. 1982, *PASP*, 94, 586
- Persic, M. & Salucci, M. 1991, *ApJ*, 368, 60
- Poggianti, B. M. 1997, *A&AS*, 122, 399
- Quilis, V., Moore, B. & Bower, R. 2000, *Science*, 288, 1617
- Richter, O.-G. & Sancisi, R. 1994, *A&A*, 290, L9
- Rubin, V. C., Waterman, A. H. & Kenney, J. D. P. 1999, *AJ*, 118, 236
- Sarazin, C. 1986, *Rev. Mod. Phys.*, 58, 1
- Solanes, J. M., Manrique, A., García-Gómez, C., González-Casado, G., Giovanelli, R. & Haynes, M. P. 2001, *ApJ*, 548, 97
- Swaters, R. A., Schoenmakers, R. H. M., Sancisi, R. & van Albada, T. S. 1999, *MNRAS*, 304, 330

Uson, J. M., Boughn, S. P. & Kuhn, J. R. 1991, *ApJ*, 369, 46

van Gorkom, J. H. 1996, in *The Minnesota Lectures on Extragalactic Hydrogen*, ed. E. D. Skillman, ASP Conference Series, Vol. 106, p. 293

Whitmore, B. C., Forbes, D. A. & Rubin, V. C. 1988, *ApJ*, 333, 542

Ziegler, B. L., Bower, R. G., Smail, I., Davies, R. L. & Lee, D. 2001, *MNRAS*, 325, 1571

Table 1. The $z \sim 0.1$ Cluster Sample

Cluster	R.A. (B1950)	Decl. (B1950)	l, b ($^{\circ}$)	cz_{\odot} (km s^{-1})	cz_{cmb} (km s^{-1})	$\sigma_{1d, \text{rest}}$ (km s^{-1})	N_z	L_X^a (10^{37} W)	R^b
A1413	115248	+233900	226,+77	42453 \pm 570	42767	1490	9	10.3 \pm 0.5	4.5 ^b
A2029	150830	+055700	7,+51	23220 \pm 170	23400	1471	92	16.4 \pm 0.6	4.4 ^b
A2218	163542	+661900	98,+38	52514 \pm 170	52497	1437	93	9.3 \pm 0.4	4.3 ^b
A2295	180018	+691300	99,+30	24623 \pm 200	24555	563	9	<0.1	0
A2670	235136	–104100	81,–69	22841 \pm 60	22494	895	235	2.0 \pm 0.1	1.4 ^b

^aMeasured over the range 0.5–4.5 keV and covering a $0.7 h_{70}^{-1}$ Mpc radius by Jones & Forman (1999).

^b“Abell richness class” re-estimated by Dressler (1978) from the redshift of these clusters. Abell’s original estimates were $R = 3$ (A1413), 2 (A2029), 4 (A2218) and 3 (A2670).

Table 2. Palomar 5 m Spectroscopy Observing Runs^a

Date	Clusters Observed	Nights Used	N_{RC}	H α Rate	Approx. Seeing ($''$)	Wavelength Coverage (\AA)	cz Range (H α) (km s^{-1})
1999 Apr 20-21	A2218	0.7 ^b	1	1/ 8	1.5–2	7250–7920	30,300–62,100
1999 May 14	A2218	1	3	4/11	1.5–2.5	7330–8000	33,500–65,700
1999 Oct 31-Nov 1	A2670	2 ^b	16	15/28	1.5–2	6780–7450	9,800–40,300
2001 May 20-21	A1413,A2218	2	7	12/31	1.5–2.5	7330–8000	33,500–65,700

^aThe data for Abell 2029 and Abell 2295 are described in Dale & Uson (2000) and Dale et al. (1998), respectively.

^bA portion of the observing run was devoted to another project.

Table 3. Target Galaxy Sample

Galaxy	R.A. (B1950)	Decl. (B1950)	cz_{\odot} (km s^{-1})	RC	Galaxy	R.A. (B1950)	Decl. (B1950)	cz_{\odot} (km s^{-1})	RC
A1413-211894	115208.1	+233828	...	0	A2218-261717	163612.6	+663031	52378	1
A1413-211903	115216.8	+235549	...	0	A2218-261274	163618.1	+662436	...	0
A1413-211916	115228.0	+235115	...	0	A2218-261718	163644.7	+661913	51601	1
A1413-211924	115238.6	+235007	42900	2	A2218-261719	163647.4	+661425	...	0
A1413-211934	115243.6	+234059	42844	0	A2218-261720	163647.5	+662135	54557	2
A1413-211938	115244.8	+234332	...	0	A2218-261286	163650.7	+662455	...	0
A1413-211956	115301.1	+234748	...	0	A2218-261721	163658.6	+660743	...	0
A1413-211957	115301.6	+234725	41400	2	A2218-261289	163700.4	+661548	...	0
A1413-211968	115331.3	+235648	...	0	A2218-261290	163705.2	+661137	...	0
A2218-261222	163237.5	+662428	...	0	A2218-261723	163752.9	+661412	...	0
A2218-261223	163248.0	+661744	56018	1	A2218-261291	163755.8	+662815	51553	1
A2218-261702	163250.8	+660732	...	0	A2670-630560	235008.6	-110012	22883	0
A2218-261224	163255.6	+663400	...	0	A2670-630563	235024.5	-105752	21810	1
A2218-261703	163302.7	+661240	...	0	A2670-630565	235031.5	-105736	21948	1
A2218-261704	163314.2	+662632	...	0	A2670-630567	235034.8	-110058	22561	1
A2218-261705	163318.4	+662500	55706	1	A2670-630568	235034.9	-104620	22892	1
A2218-261706	163340.0	+660322	...	0	A2670-630570	235044.7	-103449	22607	0
A2218-261226	163421.0	+662518	52793	1	A2670-630571	235044.9	-103944	22291	2
A2218-261708	163456.9	+663036	...	0	A2670-630574	235053.7	-104718	21843	0
A2218-261709	163502.8	+661355	...	0	A2670-630577	235111.6	-105034	23501	1
A2218-261244	163518.8	+662121	42855	1	A2670-630584	235124.6	-105820	23662	0
A2218-261245	163523.0	+661938	...	0	A2670-630585	235126.2	-103826	23757	0
A2218-261247	163524.0	+662003	...	0	A2670-630318	235129.7	-103642	20968	0
A2218-261710	163524.6	+661204	...	0	A2670-630317	235130.4	-104231	21597	1
A2218-261248	163527.3	+662630	...	0	A2670-630319	235132.2	-104208	22380	0
A2218-261711	163529.1	+662719	52572	1	A2670-630588	235134.1	-105129	22562	1
A2218-261251	163530.2	+661213	...	0	A2670-630322	235139.2	-103951	23398	0
A2218-261712	163531.1	+660345	37100	2	A2670-630593	235139.5	-104006	23924	1
A2218-261252	163532.9	+662302	...	0	A2670-630324	235142.6	-103136	22674	0
A2218-261713	163538.9	+661645	53500	2	A2670-630597	235143.0	-104138	24556	0
A2218-261259	163539.5	+661912	...	0	A2670-630599	235144.0	-104136	23128	0
A2218-261714	163545.7	+661000	...	0	A2670-630600	235144.2	-103031	23229	1
A2218-261265	163550.3	+661751	54862	0	A2670-630328	235153.3	-103855	22918	0
A2218-261715	163554.1	+661404	39100	2	A2670-630607	235153.3	-104040	27928	1
A2218-261268	163556.3	+662422	53852	1	A2670-630615	235210.2	-103337	23141	1
A2218-261269	163600.5	+661742	...	0	A2670-630621	235226.9	-102654	23605	0
A2218-261271b	163602.1	+662726	55300	2	A2670-630624	235242.7	-110249	13010	1
A2218-261271	163604.4	+662730	...	0	A2670-630625	235246.9	-103855	22361	1
A2218-261272	163611.9	+661725	...	0	A2670-630627	235255.7	-102030	12640	2

Table 4. Galaxy Spectroscopic Parameters

Galaxy	T_{exp}	cz_{cmb}	W_{obs}	i	W_{cor}
(1)	(s)	(km s^{-1})	(km s^{-1})	($^{\circ}$)	(km s^{-1})
(1)	(2)	(3)	(4)	(5)	(6)
A2218-261223	3900	56003±07	397	70	370±21
A2218-261705	4800	55690±07	538	60	530±27
A2218-261226 ^a	4500	52777±10	300	58	354±28
A2218-261244 ^a	900	42838±14	427	69	413±24
A2218-261711	4800	52555±07	426	69	409±22
A2218-261268	5700	53835±10	402	64	382±26
A2218-261717	4500	52360±07	367	65	350±23
A2218-261718	6300	51583±10	305	66	299±23
A2218-261291	3300	51534±08	398	57	441±25
A2670-630563	3600	21463±10	372	53	450±33
A2670-630565	900	21601±10	342	66	372±23
A2670-630567	1800	22215±10	528	70	521±25
A2670-630568	2400	22545±10	453	79	454±22
A2670-630571 ^a	1200	21944±10	131	54	154±31
A2670-630577	2400	23154±10	390	61	422±23
A2670-630317	1200	21250±10	323	63	352±27
A2670-630588 ^a	2400	22215±10	292	79	354±43
A2670-630593 ^a	900	23577±10	338	71	413±45
A2670-630600	3600	22882±10	443	90	432±21
A2670-630607 ^a	600	27581±10	427	72	486±26
A2670-630615	3000	22794±10	316	64	363±45
A2670-630624 ^a	300	12664±10	123	42	197±37
A2670-630625 ^a	4200	22014±10	451	70	495±33
A2670-630627 ^a	600	12293±10	204	67	222±23

Note. — Col. 2: The spectral exposure time. Col. 3: The recessional velocity of the galaxy in the CMB reference frame, assuming a Sun-CMB relative velocity of 369.5 km s^{-1} towards $(l, b) = 264.4^{\circ}, 48.4^{\circ}$ (Kogut et al. 1993). Col. 4: The observed velocity width. Col. 5: The adopted inclination i of the plane of the disk to the line-of-sight (90° corresponds to an edge-on perspective); the derivation of i and its associated uncertainty are discussed in § 4 of Dale et al. (1997). Col. 6: The velocity width at R_{opt} converted to an edge-on perspective, corrected for the shape of the rotation curve, cosmological broadening, and the smearing effects due to the finite width of the slit of the spectrograph. The uncertainty takes into account both measurement errors and uncertainties arising from the corrections.

^aSee notes on individual objects in § 3.2.

Table 5. Galaxy Photometric Parameters

Galaxy	T	θ	PA	ϵ	R_d	R_{opt}	m_I	$M_I - 5 \log h_{100}$
(1)	(2)	($'$) (3)	($^\circ$) (4)	(5)	($''$) (6)	($''$) (7)	(8)	(9)
A2218-261223	3:	18	7	0.613±0.049	2.2	6.0	17.35	-21.39±0.07
A2218-261705	2:	16	100	0.464±0.033	1.4	4.4	17.06	-21.67±0.09
A2218-261226 ^a	1	10	17	0.432±0.043	1.3	4.0	17.75	-20.86±0.10
A2218-261244 ^a	2	3	18	0.596±0.064	4.2	8.5	16.32	-21.84±0.10
A2218-261711	3:	8	0	0.581±0.040	1.2	3.7	17.72	-20.88±0.06
A2218-261268	5	6	114	0.540±0.063	1.6	5.8	17.25	-21.35±0.07
A2218-261717	3	12	45	0.535±0.040	1.8	5.0	17.50	-21.10±0.06
A2218-261718	6	6	175	0.566±0.058	1.0	3.8	17.75	-20.85±0.09
A2218-261291	2:	16	67	0.427±0.021	1.1	3.6	17.59	-20.97±0.09
A2670-630563	4	24	130	0.397±0.042	4.3	13.0	14.66	-22.00±0.05
A2670-630565	5	23	83	0.583±0.036	4.0	12.0	14.82	-21.85±0.05
A2670-630567	3	25	135	0.565±0.048	4.3	14.3	14.95	-21.78±0.07
A2670-630568	2	16	159	0.723±0.045	3.2	9.8	15.18	-21.58±0.14
A2670-630571 ^a	4	13	43	0.206±0.112	3.3	10.8	15.12	-21.64±0.07
A2670-630577	5	11	51	0.491±0.025	2.6	7.7	15.02	-21.74±0.04
A2670-630317	5	2	105	0.622±0.063	2.0	7.2	15.39	-21.37±0.05
A2670-630588 ^a	5	11	97	0.760±0.009	2.9	9.6	15.25	-21.51±0.10
A2670-630593 ^a	7	1	110	0.643±0.037	2.3	8.1	14.88	-21.88±0.05
A2670-630600	2:	11	138	0.804±0.015	4.7	14.6	15.05	-21.71±0.14
A2670-630607 ^a	5	4	145	0.664±0.018	3.2	9.2	15.50	-21.70±0.05
A2670-630615	3:	11	151	0.543±0.057	5.4	15.0	15.31	-21.45±0.07
A2670-630624 ^a	7	27	115	0.255±0.040	2.1	7.0	15.86	-19.65±0.09
A2670-630625 ^a	3	18	86	0.540±0.099	2.7	8.9	14.84	-21.92±0.08
A2670-630627 ^a	1:	28	80	0.572±0.043	5.7	14.5	14.65	-20.80±0.10

Note. — Col. 2: Morphological type code: 1 corresponds to Sa, 3 to Sb, 5 to Sc and so on. The codes are assigned after visually inspecting the I band images and noting the value of R_{75}/R_{25} , where R_X is the radius containing X% of the I band flux. This ratio is a measure of the central concentration of the flux which was computed for a variety of bulge-to-disk ratios. Given the limited resolution of the images, some of the inferred types are rather uncertain; uncertain types are followed by a colon. Col. 3: The cluster-centric distance. Col. 4: Position angle used for spectrograph slit (North: 0° , East: 90°). Col. 5: Ellipticity of the disk corrected for seeing effects as described in § 5. Col. 6: The (exponential) disk scale length. Col. 7: The distance along the major axis to the isophote containing 83% of the I band flux. Col. 8: The measured I band magnitude, extrapolated to 8 disk scale lengths assuming that the surface brightness profile of the disk is well described by an exponential function. k -corrections and allowances for Galactic and internal extinction are made. Col. 9: The absolute magnitude, computed assuming that the galaxy is at the distance indicated by the cluster redshift if the galaxy is a cluster

Table 6. Results

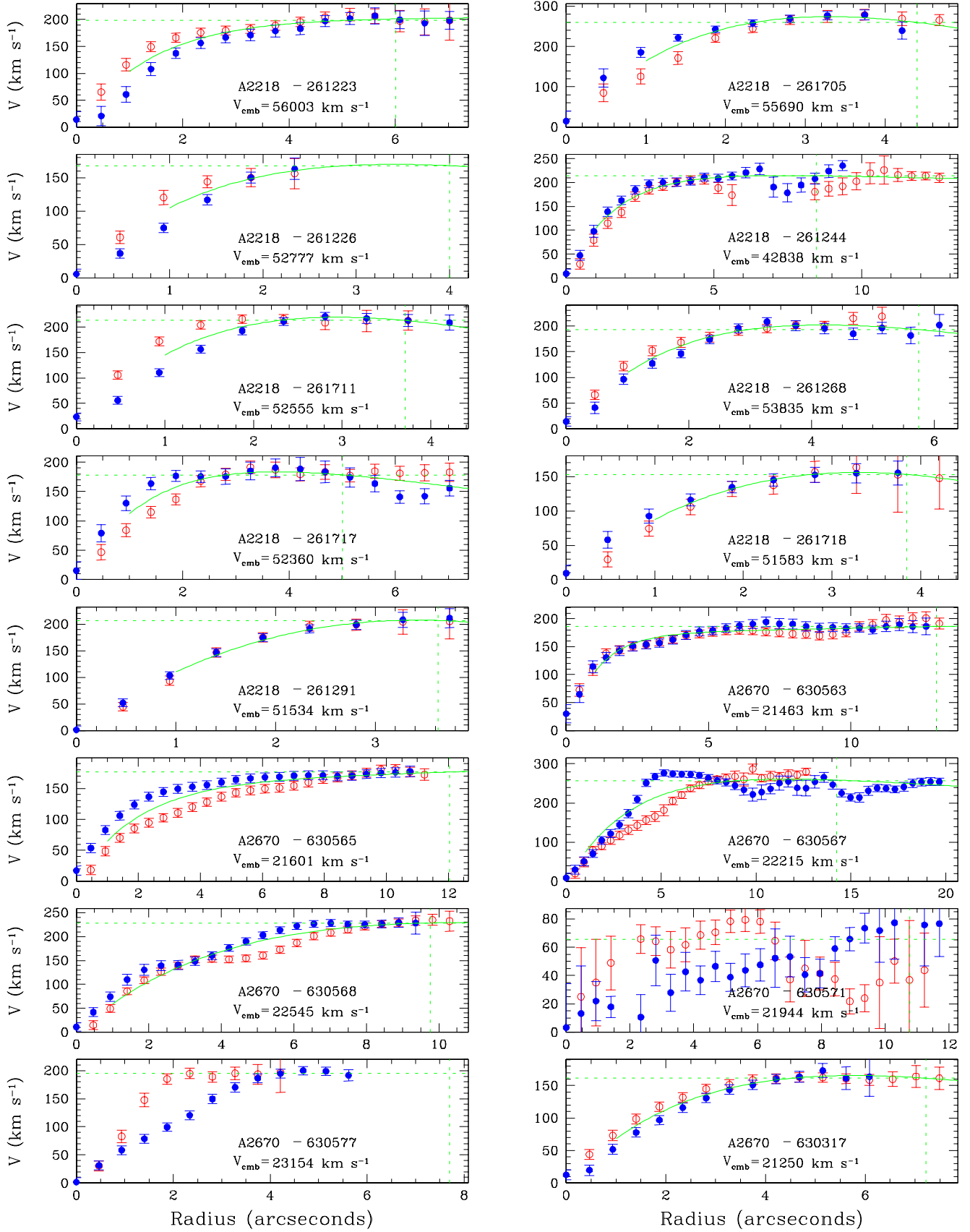
Spiral Galaxy Sample	H α Rate	Median $R_{\text{H}\alpha}$ (R_{200})	Median $R_{\text{no H}\alpha}$ (R_{200})	RC Asymm. (%)	RC Shape (%)	RC Extent (R_{opt})	H α EW (\AA)
$z \sim 0.1$ clusters	70 of 156	0.47	0.36	12.6 \pm 1.2	11.1 \pm 1.2	1.18 \pm 0.07	15.9 \pm 2.7
$T < \text{Sbc}$	10.9 \pm 1.3	10.4 \pm 2.1	1.29 \pm 0.09	12.7 \pm 2.8
$T > \text{Sb}$	13.8 \pm 1.7	11.6 \pm 1.5	1.10 \pm 0.09	17.9 \pm 4.0
$z < 0.1$ clusters	582 of 897	0.75	...	14.0 \pm 0.4	10.1 \pm 0.4	1.11 \pm 0.02	...
Field	12.5 \pm 1.0	10.6 \pm 1.1	1.18 \pm 0.04	22.8 \pm 1.3 ^a

^aDerived from the Kennicutt (1998) sample of nearby galaxies.

Table 7. Tully-Fisher Relation

Cluster	N_{TF}	$a_{\text{bias}} - a_{\text{TF}}$ (mag)	$a - a_{\text{TF}}$ (mag)	σ_a (mag)	$c z_{\text{cmb}}$ (km s ⁻¹)	$v_{\text{pec,cmb}}$ (km s ⁻¹)
A2029	14	-0.100	-0.052 \pm 0.157	0.53 (0.34)	23400	+550 \pm 1700
A2218	8	+0.237	+0.251 \pm 0.138	0.34 (0.29)	52497	-6400 \pm 3300
A2295	10	-0.042	-0.026 \pm 0.137	0.38 (0.32)	24555	+290 \pm 1500
A2670	11	+0.003	+0.012 \pm 0.116	0.32 (0.17)	22494	-120 \pm 1200

Note. — Col. 3: Tully-Fisher offset with respect to the $z \sim 0.1$ template zero point, uncorrected for cluster population incompleteness bias. Col. 4: Tully-Fisher offset with respect to the $z \sim 0.1$ template zero point, corrected for cluster population incompleteness bias. Col. 5: Tully-Fisher scatter, with the intrinsic contribution in parentheses.



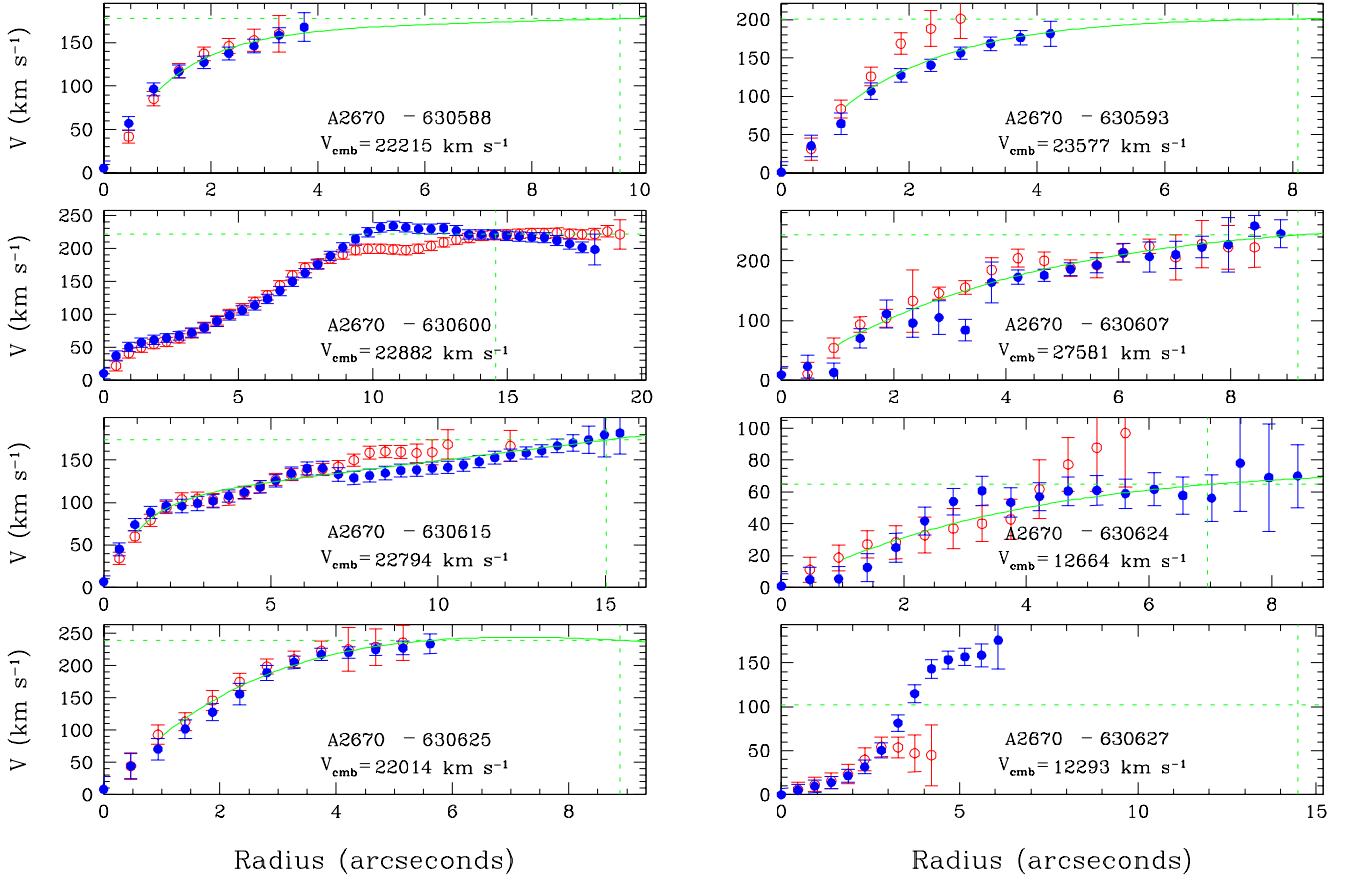


Fig. 1.— The folded rotation curves. The error bars include both the uncertainty in the wavelength calibration and the rotation curve fitting routine used. Names of the galaxy are given along with the CMB radial velocities. Two dashed lines are drawn: the horizontal line indicates the adopted half velocity width, which in some cases arises from an extrapolation to the rotation curve; the vertical line is at R_{opt} , the radius containing 83% of the I band flux. A fit to the rotation curve is indicated by a solid line. Note that the rotation curves are *not* deprojected to an edge-on orientation.

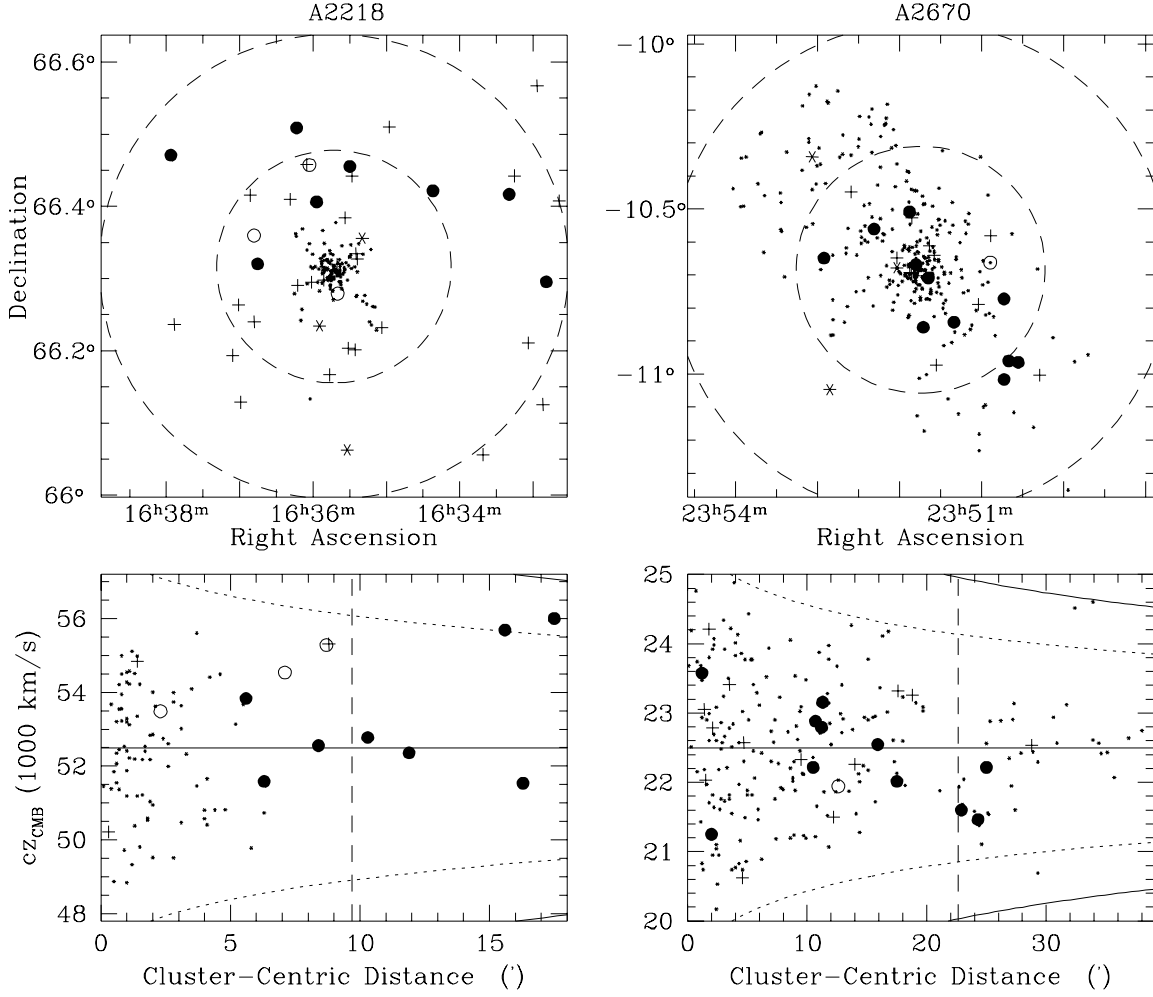


Fig. 2.— Sky and velocity distribution of galaxies in the fields of Abell 2218 and Abell 2670. Circles represent cluster members with measured photometry and widths; if unfilled, widths are poorly determined. Asterisks identify foreground and background galaxies, and dots give the location of galaxies with known redshift. Crosses indicate the positions of galaxies lacking emission lines (their redshifts are drawn from the literature). The dashed lines indicate 1 and 2 Abell radii. The dotted and solid lines respectively indicate 2 and 3 σ cluster membership contours (see Equations 8–11 in Carlberg et al. 1997, with $H_o = 70 \text{ km s}^{-1} \text{ Mpc}^{-1}$, $\Omega_o = 0.3$ and $\Omega_\lambda = 0.7$).

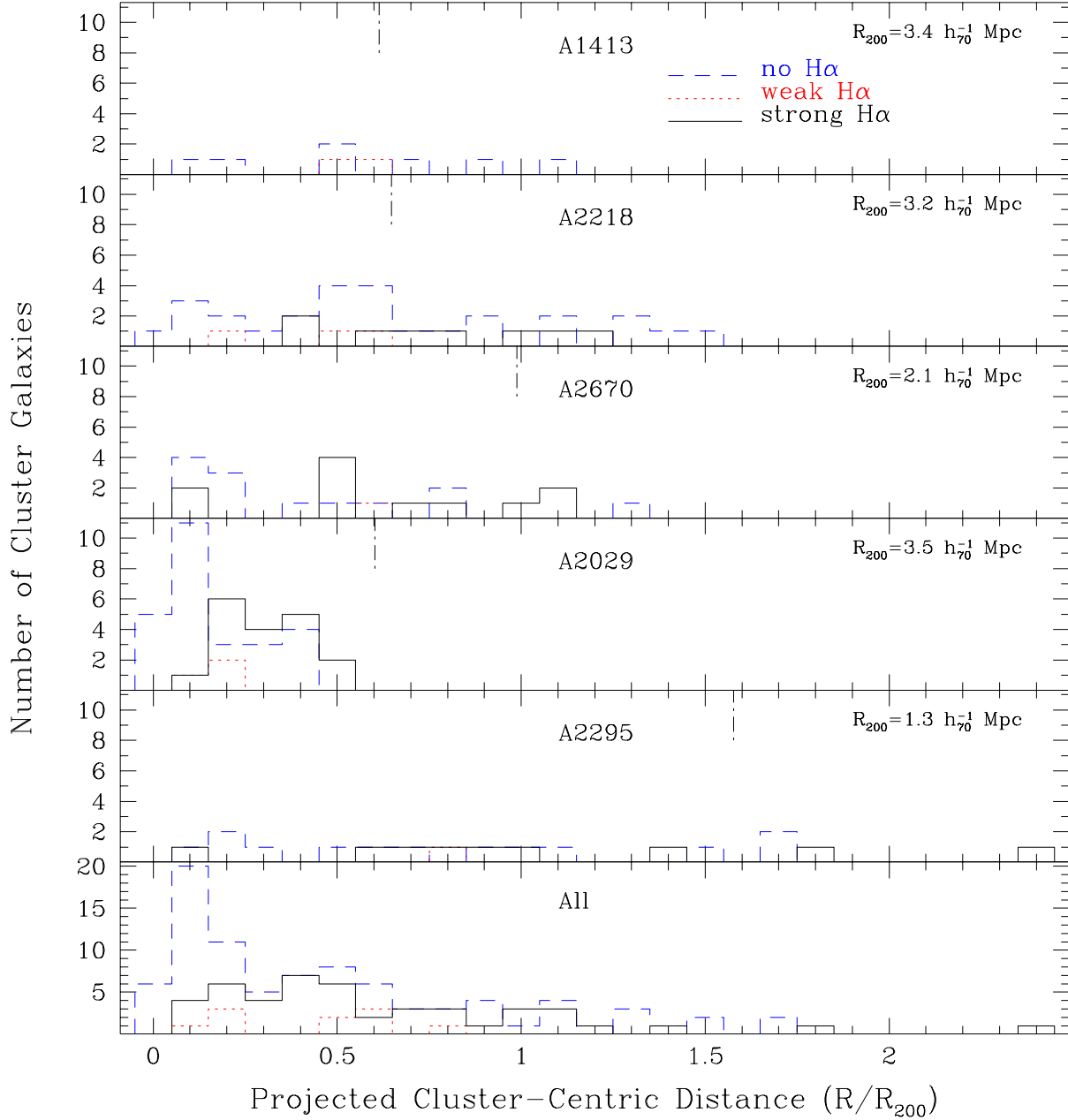


Fig. 3.— The distribution of observed cluster galaxies in Abell 1413, Abell 2029, Abell 2218, Abell 2295, and Abell 2670 (panels 1 through 5) as well as for the combined sample, as a function of the projected distance to the cluster center (in units of R_{200}), separated according to the strength of the observed H α line emission. One Abell radius is indicated by a dot-dash vertical line.

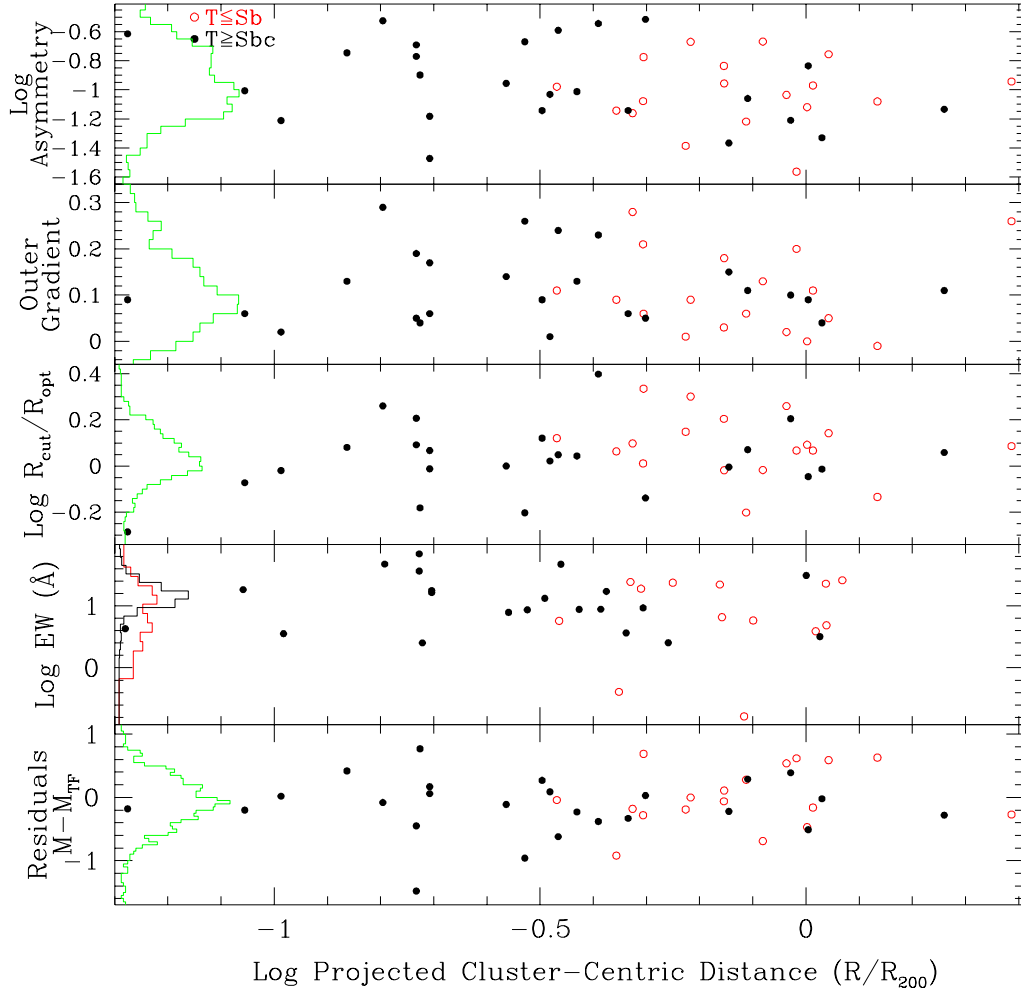


Fig. 4.— **Top panel:** Rotation curve asymmetry (Equation 1). **Second panel:** The outer gradient parameter for the rotation curves (Equation 2). **Third panel:** The maximum radial extent of the observed emission line within the disk, normalized to the semi-major axis containing 83% of the I band flux. The histograms in the top three (and bottom) panels are the distributions for 441 galaxies in 52 lower redshift Abell clusters (Dale et al. 1999). **Fourth panel:** $H\alpha$ equivalent width. Open circles indicate Sb and earlier cluster galaxies while filled circles show Sbc and later cluster galaxies. The histograms at the left are the $H\alpha$ equivalent widths found by Kennicutt (1998). The more sharply peaked histogram is for $T \geq Sbc$, while the other histogram is for $T \leq Sb$. **Bottom panel:** Residuals of the Tully-Fisher data as a function of projected cluster-centric distance (Equation 4).

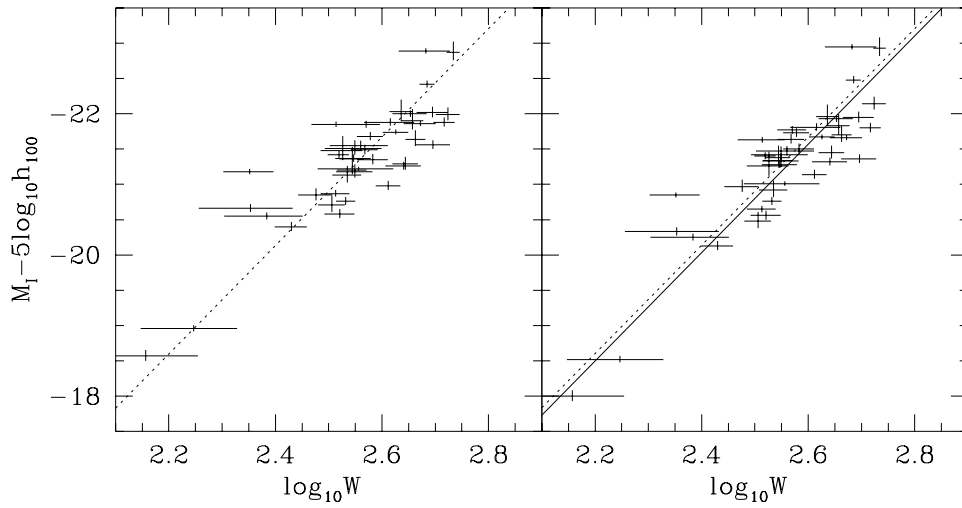


Fig. 5.— The Tully-Fisher data for Abell 2029, Abell 2218, Abell 2295, and Abell 2670. The morphological offsets advocated by Giovanelli et al. (1997) and Dale et al. (1999) have been applied to the early-type spirals: $\Delta m_T = -0.1$ mag for the Sb galaxies, and $\Delta m_T = -0.32$ mag for earlier type spirals. The data in the righthand panel are additionally corrected for cluster peculiar motion and population incompleteness bias. The dashed line in each panel is the template relation for $0.02 \lesssim z \lesssim 0.06$ clusters (Equation 3) obtained by Dale et al. (1999), whereas the solid line in the righthand panel (Equation 4) reflects the average zero point for the $z \sim 0.1$ clusters: Abell 2029, Abell 2295, and Abell 2670.